Impact of stresses and restraints on ASR expansion

Pierre Morenon, Stéphane Multon, Alain Sellier, Etienne Grimal, Francois Hamon, Eric Bourdarot

IMPACT OF STRESSES AND RESTRAINTS ON ASR EXPANSION

Pierre Morenon[1,2*], Stéphane Multon[2], Alain Sellier[2], Etienne Grimal[1], François Hamon[3], Eric Bourdarot[1]

[1]Electricité de France, Centre d'Ingénierie Hydraulique, EDF-CIH Technolac, 73373 Le Bourget du Lac Cedex France

[2]LMDC, Université de Toulouse, INSA/UPS Génie Civil, 135 Avenue de Rangueil, 31077 Toulouse cedex 04 France

[3]EDF Lab Paris – Saclay, 7 boulevard Gaspard Monge Bureau 02-B07 91120 Palaiseau - France

Abstract

Some large civil engineering structures, principally certain concrete dams, are subject to the structural effects of Alkali-Silica Reaction (ASR). Due to the directions of loading and reinforcement, the stress state is mostly anisotropic. The aim of this paper is to describe the impact of applied stresses and restraint due to reinforcement or boundary conditions on ASR-expansion and induced anisotropic cracking. After the definition and validation of the poromechanical modelling, the paper gives a detailed description of the effects of different aspects of stress (in one, two or three directions) and reinforcement on ASR-expansion for engineers in charge of damaged structures.

Keywords: Alkali-Silica Reaction, concrete modelling, stresses effects, anisotropy, damage

Highlights:

Impacts of applied stresses and restraints on ASR-expansion are compared.

The anisotropy of expansion is induced by the resolution of the mechanical equilibrium between stresses and the isotropic pressure of ASR-gel using a cracking criterion.

* Corresponding author. E-mail address: morenon@insa-toulouse.fr (P. Morenon). LMDC, Université de Toulouse, INSA/UPS Génie Civil, 135 Avenue de Rangueil, 31077 Toulouse cedex 04 France Tel.: +33 5 61 55 99 16 - Fax. : +33 5 61 55 99 49.

The model is calibrated and validated on experimental results under multi-axial loading and restraints.

Theoretical tests were conducted in order to analyse the model response (strains, stresses and gel pressure) under several kinds of loading (multi-axial compression, unloading and tension).

Reinforcement induces concrete prestress and anisotropic cracking.

1. Introduction

Alkali-silica reaction (ASR) occurs on structures that contain some specific siliceous reactive aggregates. Engineers discovered this pathology through the observation of cracking on basements. Among large civil engineering structures, concrete dams, in particular, are subject to structural effects caused by ASR [1–4]. This is mainly attributable to the concrete composition and climatic conditions such as water supply. These swellings can lead to damage and cracks on structures and result in a decrease of their stability.

The main aim for dam owners is to ensure the safety of the population while optimizing maintenance. Many authors are working on ASR modelling in order to predict the long-term behaviour of affected structures [5–9]. Relevant modelling can also anticipate the choice of options during repairs.

ASR expansion occurs in structures that sustain significant loads, such as bridge piers, or are restrained by external loading conditions, such as dams in valleys. Restraining expansion by reinforcement and prestressing in structures also causes stresses during expansion. In order to manage the damaged structures, owners need reliable tools to predict future damage. Stress free ASR swelling has been largely studied and several models reproduce the phenomenon realistically. Despite the number of experiments, ASR swelling under restraint is not yet fully understood and modelled.

The aim of the present paper is to describe the impact of applied stresses and stresses induced by restraints due to reinforcement or boundary conditions on ASR-expansion and anisotropic cracking. In the model, the anisotropy of expansion is not introduced through chemical loading with empirical relationships but by the resolution of the mechanical equilibrium between stresses (due to external loading, prestressing, or restraint and boundary conditions) and the isotropic pressure of ASR-gel, through a cracking criterion assessed in the three main directions. An anisotropic stress state will induce anisotropic cracking and, as a result, anisotropic expansion. After a description of the model, parameters are fitted and validated on multi-axial restrained experiments drawn from the literature [10]. Based on this calibration, a parametric study is conducted to assess the multi-axial behaviour of affected concrete in various loading and unloading conditions. Then, tests are performed on steel bars and rings embedded in concrete cylinders in order to assess the impact of usual reinforcement on anisotropy swelling. Maximum stresses and damage are observed with particular attention in all tests to obtain practical considerations useful for engineering. This study shows what impact of stresses can be expected in restrained and in reinforced or prestressed structures subjected to ASR expansion. It also highlights the risks of misanalysing experimental results obtained on cores drilled from structures.

2. Constitutive equations

2.1. Rheological model

In this work, the concrete behaviour is modelled in the poro-mechanical framework. The model comprises a damage model (inspired from [11]), and a rheological model [12], in order to consider realistic interactions between ASR, creep, shrinkage and damage so as to reproduce the mechanical effects occurring in real structures.

Concrete cracking is described by a non-linear model using anisotropic plastic criteria and damage [11]. The model has recently been improved to calculate plastic strains. Two groups of criteria have been added (Fig. 1): one to manage shear cracking (Drucker Prager criteria), which is an isotropic scalar, and one to represent tension behaviour (Rankine criteria), which is an orthotropic tensor. Shear cracking is used to reproduce concrete behaviour in compression [11]. The tension criterion separates structural macro-cracks, reclosing macro-cracks (tension cracking in Fig. 1) and intra-porous pressure micro-cracks (ASR) by considering the gel pressure P_g.

The creep model, a Burger chain (Fig. 1), has been clarified and implemented in a poro-plastic framework [12]. Reversible creep is modelled with a Kelvin-Voigt floor and the Maxwell module (irreversible creep) uses an anisotropic formulation of the viscous strains in order to reproduce multi-axial consolidation of the material. Concrete shrinkage can also be taken into account through the water pressure P_w thanks to the poro-mechanical framework (Fig. 1).

The total stress is calculated by using the damage and the effective stress (1). The latter is obtained by considering the difference between the effects of gel and water on the solid skeleton (Fig. 1 and (2)). In the poromechanical framework, gel pressure, P_g, and water pressure, P_w, are impacted by Biot coefficients [13], respectively b_g and b_w, for the ASR-gel pressures and the water pressure inducing shrinkage. The effective poromechanical stress increment $\dot{\tilde{\sigma}}_{ij}{}'$ is calculated from the stiffness matrix S_0 and the elastic strain obtained from the total strain increment $\dot{\varepsilon}$, the plastic increment $\dot{\varepsilon}_{pl}$, the creep increment $\dot{\varepsilon}_{cr}$ and the thermal increment $\dot{\varepsilon}_{th}$ (3).

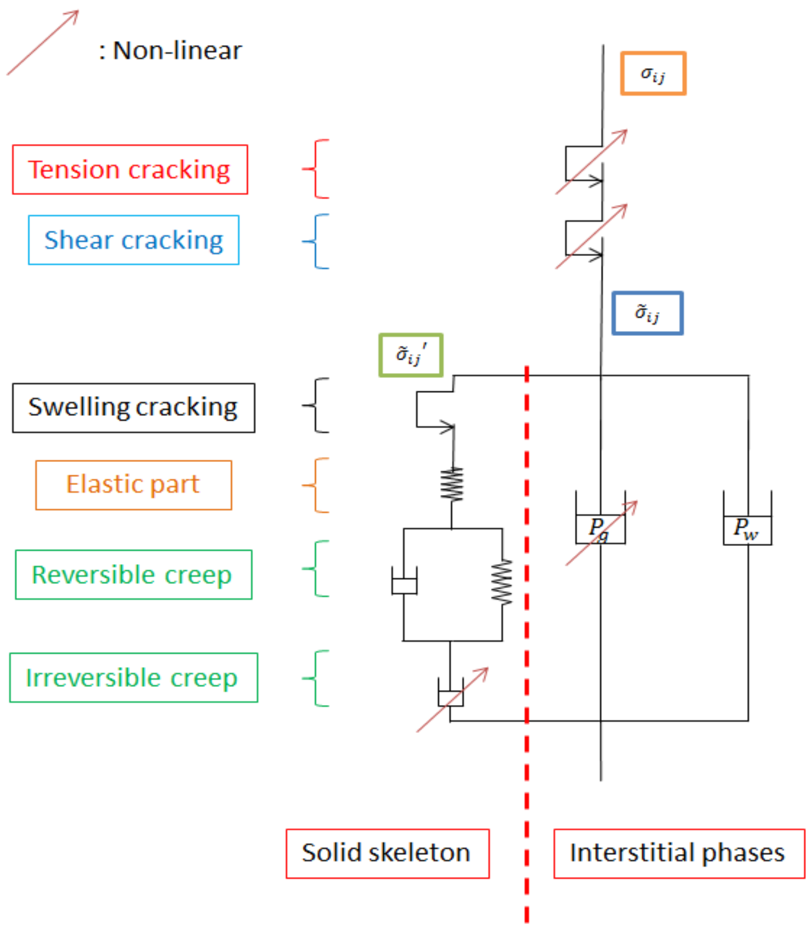

Fig. 1. Rheological scheme of the model.

$$\sigma_{ij} = (1 - D)\tilde{\sigma}_{ij} \tag{1}$$

$$\tilde{\sigma}_{ij} = \tilde{\sigma}_{ij}' - b_g P_g - b_w P_w \tag{2}$$

$$\dot{\tilde{\sigma}}_{ij}' = S_0 \left(\dot{\varepsilon} - \dot{\varepsilon}_{pl} - \dot{\varepsilon}_{cr} - \dot{\varepsilon}_{th} \right) \tag{3}$$

This paper focuses on ASR modelling, including ASR pressure and kinetics and their links to anisotropic cracking. The other aspects of the model, such as the formulation of the visco-plastic creep model, are detailed in [12], independently of the new developments reported below.

2.2. ASR model

2.2.1. Chemical advancement

ASR advancement A^{asr} varies from 0 (before the start of the reaction) to 1 (when the reaction ends). Its evolution principally depends on the temperature and the humidity of the material (4). The chemical advancement must be determined in order to evaluate the evolution of ASR-gel pressure. It depends on the characteristic time of the reaction τ_{ref}^{asr} (a material parameter), the temperature coefficient $C^{T,asr}$, the humidity coefficient $C^{W,asr}$, the maximum value of the advancement $A^{asr\,\infty}$ and the advancement itself A^{asr}.

The effect of temperature on advancement $C^{T,asr}$ is managed by an Arrhenius law (5). Two material parameters define the impact of temperature: the activation energy for ASR kinetic E^{asr} (≈ 40,000 J/Mol [14]) and the reference temperature T_{ref} for which τ_{ref}^{asr} was set.

The effect of humidity on advancement, $C^{W,asr}$, is described through a power law (6). S_r represents the saturation degree and $S_r^{th,asr}$ the humidity threshold below which the reaction stops. When the material is not saturated, the reaction kinetics slows down - and it stops totally in very dry concrete.

Finally only four material parameters are used to manage ASR advancement according to environmental conditions: τ_{ref}^{asr} (characteristic time of AAR), $S_r^{th,asr}$ (water saturation rate minimum threshold), E^{asr} (activation energy for AAR kinetics) and T_{ref} (reference temperature of τ_{ref}^{asr} fitting).

$$\frac{\delta A^{asr}}{\delta t} = \frac{1}{\tau_{ref}^{asr}} C^{T,asr} C^{W,asr} (A^{asr\,\infty} - A^{asr}) \tag{4}$$

$$C^{T,asr} = \exp\left(-\frac{E^{asr}}{R}\left(\frac{1}{T} - \frac{1}{T_{ref}}\right)\right) \tag{5}$$

$$C^{W,asr} = \begin{cases} \left(\dfrac{S_r - S_r^{th,asr}}{1 - S_r^{th,asr}}\right)^2 & if \quad S_r > S_r^{th,asr} \\ 0 & if \quad S_r \leq S_r^{th,asr} \end{cases} \tag{6}$$

2.2.2. *Gel pressure*

The fraction of gel produced by the reaction per m^3 of concrete is ϕ_g. It is the product of the advancement A^{asr} and the maximum gel potential ϕ_g^∞ , which is a characteristic of the material (7).

$$\phi_g = \phi_g^\infty . A^{asr} \tag{7}$$

Gel exerts a pressure P_g (8) on aggregate and concrete. In this model, a macroscopic approach is used and P_g is the average pressure assumed to be transferred by the aggregate to the concrete. It mainly depends on the accessible porosity, the initial porosity or that created by strains (elastic or plastic).

$$P_g = M_g \left(\phi_g - \left(\phi_g^v \left(\frac{P_g}{\tilde{R}_I^t}\right) + b_g tr(\varepsilon^e + \varepsilon^{cr}) + tr(\varepsilon^{p,g})\right)\right) \tag{8}$$

ϕ_g^v is the fraction of gel not effective in creating expansion under characteristic pressure fixed at the effective tensile strength $\tilde{R}_I^t$ (gel that is non-swelling for chemical reasons, or gel migrating to available porosity). For a specimen in free swelling conditions, when the gel pressure P_g reaches $\tilde{R}_I^t$, micro-cracking of the concrete element begins. In cases of constrained swelling, the pressure needed to start cracking rises because it is partially balanced by the external stress as explained below. Then, the gel amount (which migrates into the connected porosity of the concrete) increases. It leads to delayed, anisotropic cracking. The management of these aspects will be clarified in the section related to the modelling of ASR cracking.

M_g is the gel Biot modulus, which is obtained from a poromechanical definition (9). Φ is the initial porosity. K_s is the skeleton bulk modulus defined by the Young's Modulus and the Poisson coefficient (10). b_g is the Biot coefficient, which is obtained from poromechanical considerations [13].

$$\frac{1}{M_g} = \frac{\Phi - b_g}{K_s} + \frac{b_g}{K_g} \tag{9}$$

$$K_s = \frac{E}{3(1-2\nu)} \tag{10}$$

Several authors have tried to measure the gel bulk modulus K_g (9) or the gel Young's Modulus E_g. Table 1 summarizes these results and proposes a corresponding Gel Biot modulus M_g obtained from equations (**9**) and (**10**). Here, M_g is equal to 27.7 GPa, which leads to K_g equal to 4.8 GPa (more than twice the modulus of water).

	Author(s)	Accessible data	M_g calculated (Equations 10 and 11)
Experimental	[15]	K_g from 24.9 to 34 GPa	From 90 to 110 GPa
	[16] [17]	E_g from 7 to 45 GPa, $0.16 < \nu < 0.22$	From 20 to 80 GPa
	[18]	K_g equals 2.2 GPa (close to the water bulk modulus)	13.5 GPa
Modelling values	[19]	-	21.7 GPa
	[7]	-	27.7 GPa

Table 1. Gel Biot modulus M_g from the literature.

In the modelling, the gel pressure P_g (8) is managed by two main parts. The first one is the non-effective gel volume, $\phi_g^v\left(\frac{P_g}{\tilde{R}_I^t}\right)$. When $P_g > \tilde{R}_I^t$ (triaxial restraint for example), the gel spreads over the connected porosity under pressure and little expansion is observed on all ASR expansion curves. The second part of the expression is the volume $b_g tr(\varepsilon^e + \varepsilon^{cr})$, which represents the porosity created by elastic and creep strains and that absorbs a part of the gel without creating pressure. The entire volume created by strains (except the ASR plastic volume, which represents the volume of cracks due to ASR) is multiplied by the Biot coefficient b_g, which comes from poromechanical considerations [13] as $b_g tr(\varepsilon)$ represents the variation of the porosity volume filled by ASR-gel under concrete strain. Grimal's model [7,11] gives a calibration of $\mathrm{b_g}$ lying between 0.1 and 0.4. For the volume of cracks induced by ASR (and represented by plastic strains $\varepsilon^{p,g}$ in this model), $\mathrm{b_g}$ equals 1 because cracks created by the gel are assumed to be always totally accessible for the gel, here, and thus completely filled (Table 2).

Free swelling	Swelling under structural strain	Swelling under structural strain and ASR micro-cracking

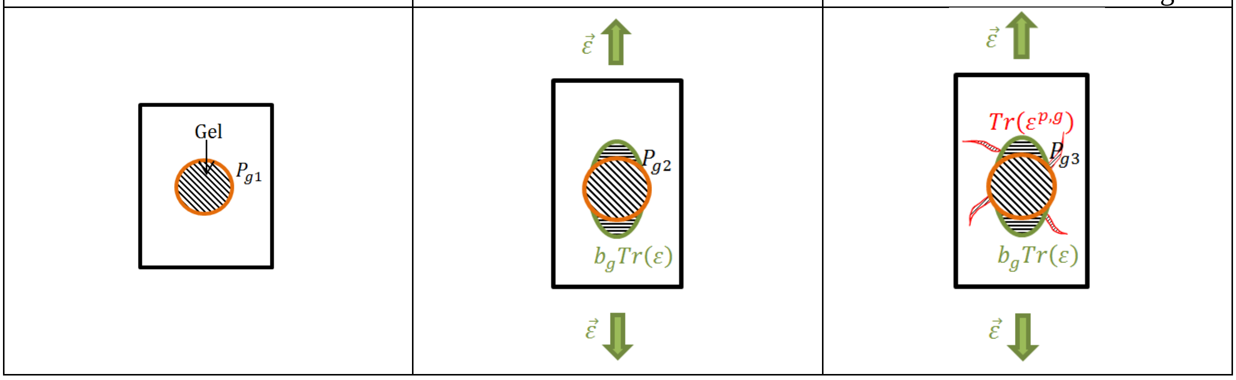

For A^{aar} = constant, $P_{g1} > P_{g2} > P_{g3}$

Table 2. Strain effects on gel pressure. $\boldsymbol{b_g tr(\varepsilon)}$ is the variation of the porosity due to concrete strain. $\boldsymbol{tr(\varepsilon^{p,g})}$ is the variation of the porosity due to plastic ASR-cracking (taken to be plastic strains in this model).

To conclude this part on gel pressure, four parameters have to be fitted on the model: the maximum gel potential, ϕ_g^∞; the fraction of non-effective gel, ϕ_g^v; the stress concentration factor, k_g; and the Biot coefficient, b_g.

2.2.3. Modelling of ASR cracking

In this model, the cracks created by ASR are represented by plastic strains. When specimens are subjected to drying shrinkage after ASR expansion, the shrinkage strains are the same as for specimens without ASR before drying [20]. During shrinkage, the strains are not modified by the previous expansions, which can thus be represented by irreversible plastic strains. The swelling difference between aggregates and paste induces a shift between lips, which leads to irreversible plastic strains even when the pressure changes in ASR-gels.

P_g is used to determine micro-cracking due to ASR by a special criterion f_I^g, which takes the stress state into account (11). $\tilde{\sigma}_I$ is the principal tensile stress in direction I.

$$\begin{cases} \mathrm{f}_\mathrm{I}^\mathrm{g} = \mathrm{P_g} & if \quad \tilde{\sigma}_\mathrm{I} \geq \tilde{\mathrm{R}}_\mathrm{I}^\mathrm{t} \\ \mathrm{f}_\mathrm{I}^\mathrm{g} = \mathrm{P_g} + \tilde{\sigma}_\mathrm{I} - \tilde{\mathrm{R}}_\mathrm{I}^\mathrm{t} & if \quad \tilde{\sigma}_\mathrm{I} < \tilde{\mathrm{R}}_\mathrm{I}^\mathrm{t} \end{cases} \text{with I} \in [\text{I,II,III}] \tag{11}$$

The hardening law that links ASR pressure to ASR strain can be drawn with a bilinear curve (Fig. 2). K_s represents the bulk modulus, $\mathrm{E_c}$ represents the concrete Young's modulus and $\mathrm{h_{asr}}$ the plastic hardening ratio ($\mathrm{h_{asr}}$.Ec is the hardening modulus). $\mathrm{h_{asr}}$ is less than 0.05 and may be determined by analysing the results of low stress state experiments. These results come from the analysis of beams studied by Multon et al. [20].

During free swelling, when the gel pressure reaches R_t, ASR induces the creation of micro-cracks that are filled by the gel. The corresponding strains are modelled using plastic strains. A coefficient h_{asr} close to 0 means that, when R_t is reached, plastic ASR strains rise very quickly with a slight increase of pressure (as $\mathrm{P_g}$ is proportional to h_{asr}). If h_{asr} is not zero, the evolution of ASR plastic strains is possible only if the gel pressure increases, and the micro-cracking induced by the gel is stable.

This quantification of the micro-cracking also expresses the fact that ASR-cracks do not appear for exactly the same advancement in all aggregates in stress free conditions. In reality, heterogeneity of ASR-cracking can be observed due to variations of tensile strength in the concrete, which lead to progressive cracking with increasing gel pressure. The plastic hardening law provides a good simplified representation of this phenomenon.

In free swelling tests, the plastic criterion (11) is reached in all directions at the same time and cracks appear in all directions (Fig. 3). However, once specimens are loaded, cracking is oriented perpendicularly to the loading direction (Fig. 3). The anisotropy of cracking leads to the expansion anisotropy that is usually observed. This is obtained by Eq. (11 in the model, in which compressive stress delays cracking (while tensile stress can accelerate it) in the loading direction. With Eq. (11, when a compression stress is applied to concrete ($\sigma < 0$), cracking first appears in a direction perpendicular to the loading (directions II and II in Fig. 3). Then, P_g increases, depending on the value of h_{asr}. If $\widetilde{\mathrm{R}}_{\mathrm{I}}^{\mathrm{g}} - \sigma$ can also be reached in the loaded direction, cracking can also be initialized perpendicular to this direction (major principal direction in Fig. 3).

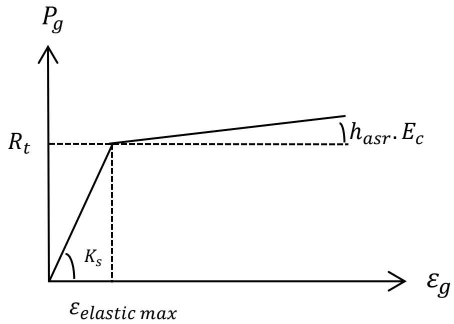

Fig. 2: Plastic ASR hardening law

Kagimoto et al. [21] cast a beam with external steel beams to restrain displacement. The crack pattern (Fig. 4) shows a usual main cracking direction (the direction of the steel bars). However, one crack is perpendicular to the main cracks. In reinforced structures, stress is induced by the gel pressure itself and P_g increases slowly. The ASR plastic criterion is the first to be reached because $\widetilde{\sigma}_{\mathrm{I}}(= b_g P_g)$ is smaller than $\mathrm{P_g}(= \widetilde{\mathrm{R}}^{\mathrm{t}}\ )$ with $b_g < 1$. The material is in compression but not enough to prevent cracks from occurring, so it can crack due to gel pressure perpendicular to the reinforcement. Larive [14] applied external compression stress to a sample but the applied stresses (5 and 10 MPa) seem to have been too high for cracks to be observed perpendicular to the applied stress direction.

Numerically, swelling is evaluated through $Tr\left(\varepsilon_{pl}{}^{g} + \varepsilon_{creep}{}^{g}\right)$ (which expresses the plastic strains (cracking) and the creep strains induced by the gel), and through the elastic strain induced by ASR swelling (12).

$$Volumic\ ASR\ strain = Tr\left({\varepsilon_{pl}}^{g} + {\varepsilon_{creep}}^{g}\right) + \frac{b_g P_g}{\left(\frac{E}{3(1-2\nu)}\right)} \quad (12)$$

2.2.4. ASR anisotropic damage

ASR damage is anisotropic. It is calculated from ASR plastic strains $\varepsilon_I^{pl,isr}$ and a material parameter to calibrate damage kinetics $\varepsilon^{k,isr}$(13).

$$D_I^{t,isr} = \frac{\varepsilon_I^{pl,isr}}{\varepsilon_I^{pl,isr} + \varepsilon^{k,isr}} \quad (13)$$

$\varepsilon^{k,isr}$ has been calibrated to approximately 0.3% [22]. The damage matrix due to ASR is a diagonal matrix which principal directions are $\varepsilon_{I,II,III}^{pl,isr}$.

The ASR compression damage matrix is obtained from the ASR tension damage matrix (14). ASR tension damage in principal directions *II* and *III* has an impact on ASR compression damage in principal direction *I*. Furthermore, when three orthogonal cracks are created, only one can be closed by external uniaxial loading.

$$D_I^{c,isr} = 1 - \left(\left(1 - D_{II}^{t,isr}\right)\left(1 - D_{III}^{t,isr}\right)\right)^{\alpha} \quad (14)$$

α is a coefficient (nearly 0.15 in flexion tests [23]) that links compression and tension ASR damage (validated on experimental tests [24]). These two types of damage are included in the total stress formula (1).

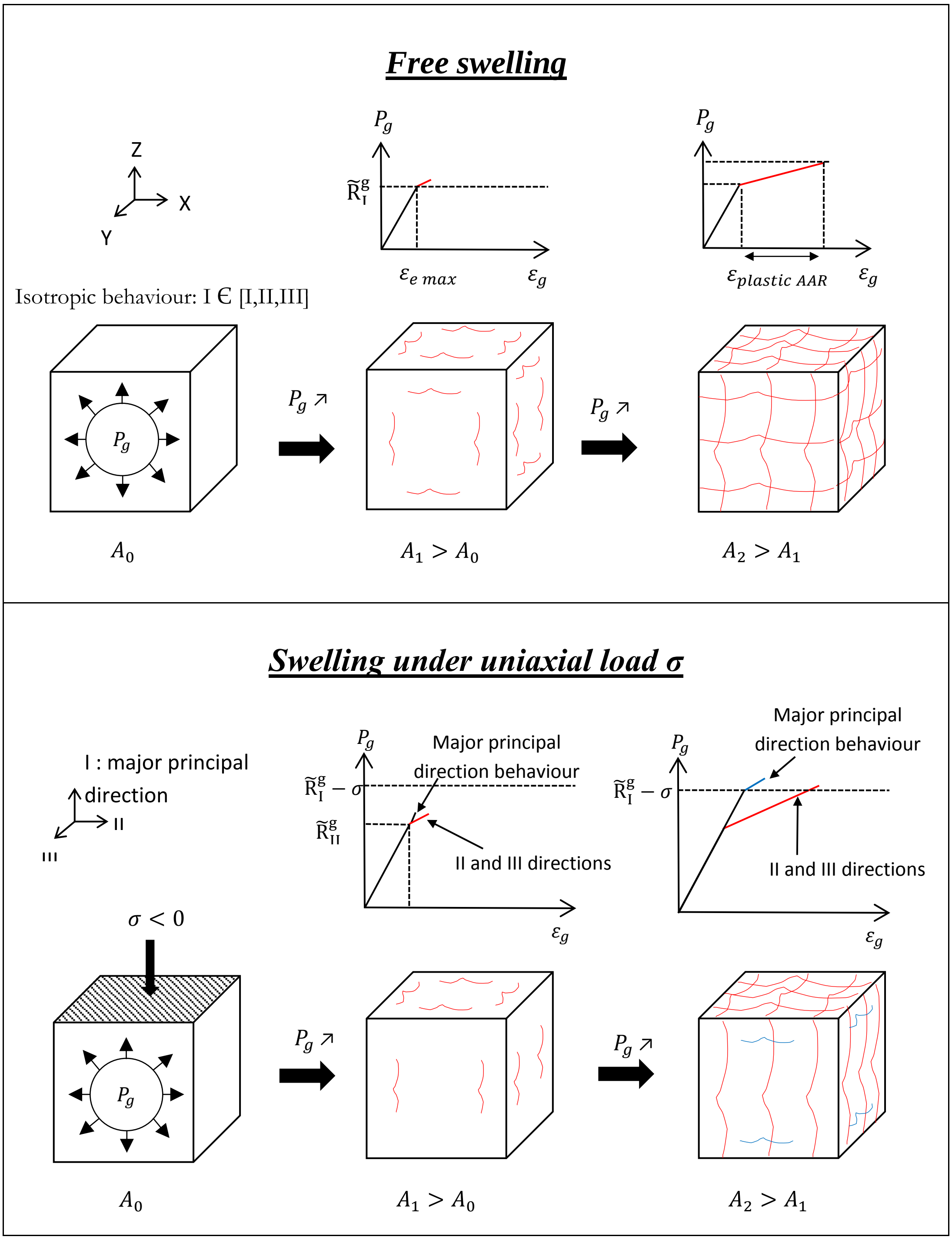

216 Fig. 3. Cracking kinetics in free swelling and in loading tests.

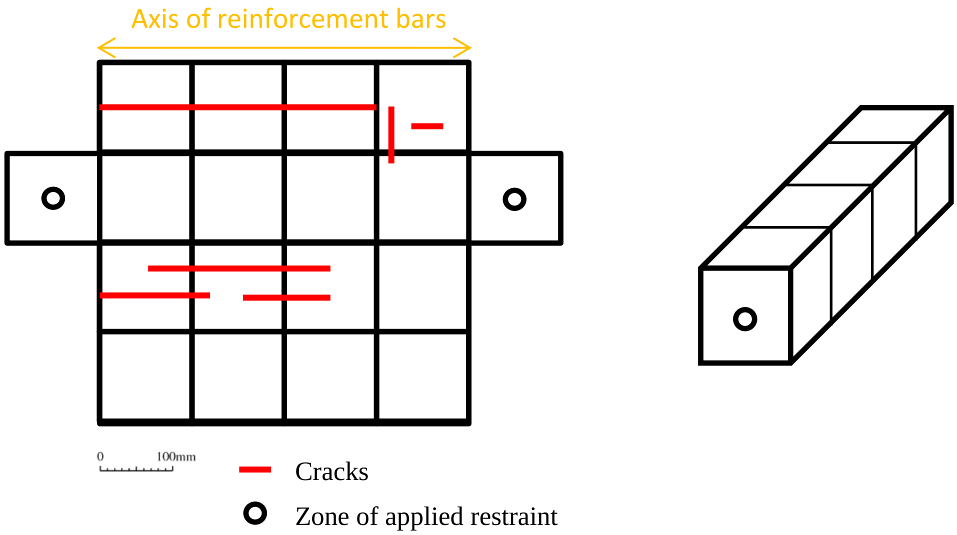

Fig. 4. Unfolded diagram of crack patterns in a concrete prism [21].

Table III summarizes the ASR model parameters.

Parameter	Symbol
Advancement	
ASR characteristic time	τ_{ref}^{asr}
Thermal activation energy	E^{asr}
Saturation degree threshold	$S_r^{th,asr}$
Poromechanics	
Maximum gel potential	ϕ_g^{∞}
Fraction of gel not effective in creating expansion	ϕ_g^{v}
Gel Biot coefficient	b_g
Gel Biot modulus	M_g
Cracking	
Plastic hardening ratio	h_{asr}

Table 3. ASR model parameters.

3. Validation and analysis of Multon's test

3.1. Experimental conditions

Numerical results were compared to the results of Multon's tests [10] in order to validate the model. In this experiment, specimens were loaded in uniaxial compression and the radial displacement was restrained by steel rings surrounding the concrete cylinders (Fig. 5). After fitting creep and shrinkage on non-reactive material, the first step was the calibration of ASR parameters. A global calibration was performed to validate the model with all restraints and loads.

During these experiments, a 28 days curing period was applied at 20°C. Then, the temperature was increased to 38°C. Results are presented after the curing period. Shrinkage cylinders were sealed with three layers of aluminium foil but they still showed a mass loss [10].

Before fitting material parameters, some physical values were measured: the tension strength and Young's Modulus were equal to 3.7 MPa 37.2 GPa respectively.

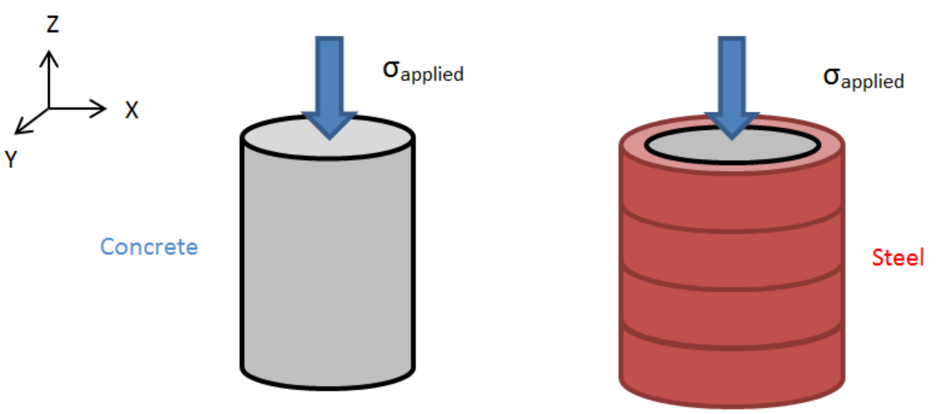

Fig. 5. Scheme of Multon's tests.

3.2. Calibration methodology

Creep and shrinkage were first calibrated on a non-reactive specimen (Fig. 6). From the mass loss, the environmental conditions and the fitting strains were reproduced faithfully through the Van Genuchten law (two material parameters M_{sh} and b, Eq. 15 [25]. Then, creep tests at 10 and 20 MPa simulated the material behaviour under long-term uniaxial loading. Four parameters were necessary to fit the creep: two characteristic times for reversible and irreversible creeps, one for the modulus of the reversible part and one characteristic strain for the irreversible part.

$$P_w = M_{sh}\left(1 - S_r^{\left(1-\frac{1}{b}\right)}\right)^{(1-b)} \tag{16}$$

During the first days of experimentation in the steel rings test, lateral concrete strains were negative, meaning that the concrete and steel were no longer in contact. To avoid initial cracking or use of an interface law, the Young's Modulus of the steel rings was numerically set close to zero until strains became positive again.

Then, the maximum gel volume, $\phi_{\mathrm{g}}^{\infty}$, and the fraction of non-effective gel, $\phi_{\mathrm{g}}^{\infty}$, were calibrated by a free swelling test. Tests with steel rings put the material in multi-axial restraint. In this state, the gel Biot coefficient, $\mathrm{b_g}$, was fitted.

3.3. Calibration analysis

Fig. **6** shows that the model was able to reproduce ASR expansions under multi-axial loads and restraints, and to approach most of the experimental results obtained in Multon's experiments.

For free swelling tests (without steel rings, marked (b) in Fig. **6**), isotropic unloaded (brown) and longitudinally loaded (blue and red) swelling curves were fitted; the behaviour was well reproduced. Transversally (yellow and green curves), the kinetics given by the model was a little fast. At the asymptote, the 20 MPa case was correctly reproduced but 10 MPa final strain was too high. Experimentally, unloaded strain and transversal 10 MPa strain were quite similar while the loaded strain was expected to be higher than the unloaded one (due to the Poisson effect).

For restrained tests ((c) and (d) in (Fig. **6**), loaded tests were reproduced faithfully. Transversally, stress free tests were well simulated (black curves). Longitudinally, the kinetics was a little fast. Final strain was correct for the 5 mm test (dark blue curve on (d)) but too high for the 3 mm test (dark blue curve on (c)). These experimental points seem to be very different in the 3 and 5 mm tests whereas values are close for all other tests with steel rings.

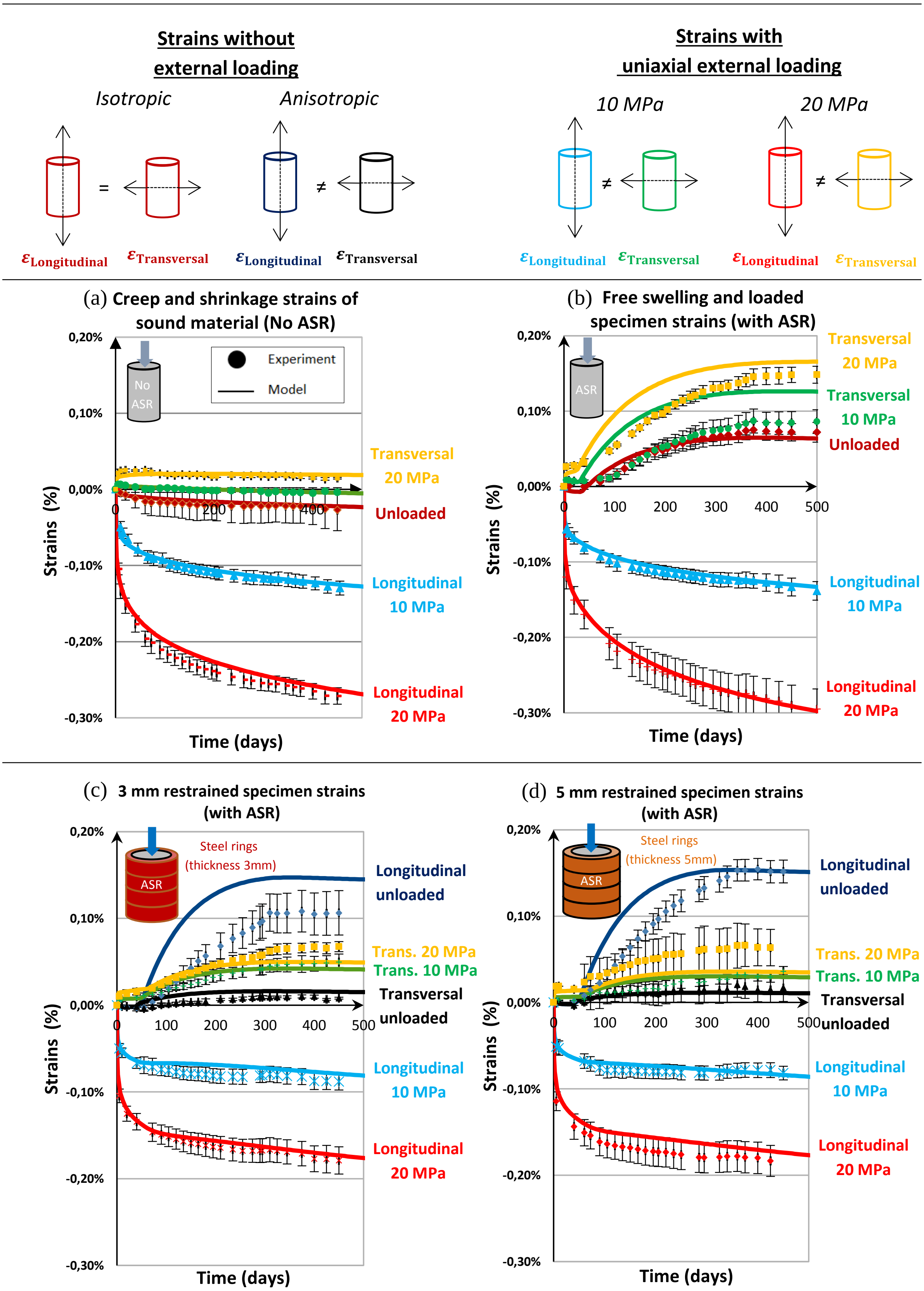

Fig. 6. Multon's test results for strains [10] : (a) creep and shrinkage without ASR, (b) ASR free swelling tests and loaded tests, (c) 3 mm restrained tests, (d) 5 mm restrained tests (R_t=3.7 MPa; $\boldsymbol{\phi}_g^{\infty}$=0.0054 m^3/m^3; $\boldsymbol{\phi}_g^{v}$=0.0013 m^3/m^3 b_g=0.25; M_g=27700 MPa; h_{asr}=0.03)

Due to ASR expansion and the Poisson effect on loaded tests, radial stresses developed on these rings. These stresses were extracted from the calculations (Fig. 7). Model results gave radial stresses between 1.2 and 5.4 MPa (compression stresses). Radial stress curves contained four parts: the application of external stress (between 0 and 1 day), the latency period before expansion became significant (between 1 and 80 days), the expansion period (between 80 and 350 days) and the part where the reaction was over and shrinkage became the main deformation phenomenon.

During the latency period, radial stress was nearly zero for unloaded specimens because shrinkage was greater than the gel pressure, so the concrete and the steel rings were not in contact. Specimens with 3 mm thick steel rings showed smaller radial stress than specimens with 5 mm thick rings because of the difference of rigidity.

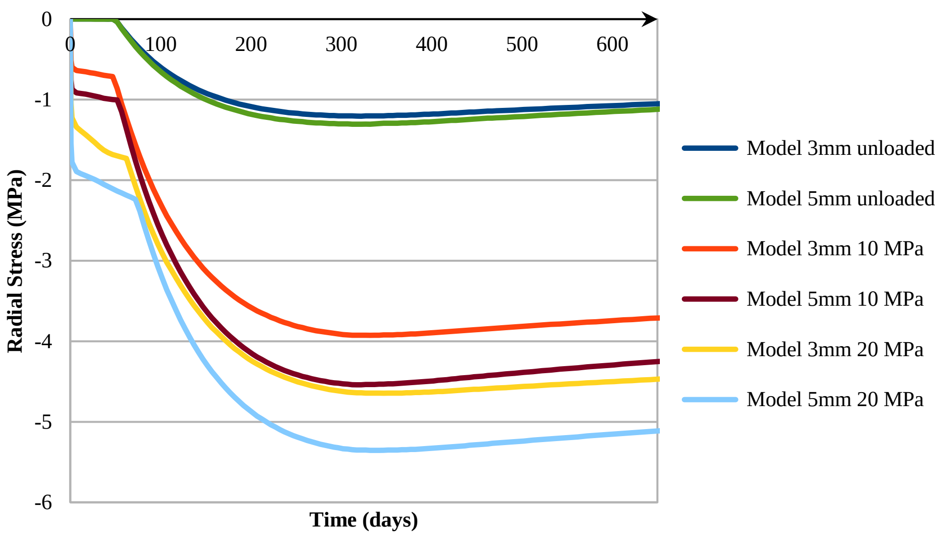

Fig. 7. Radial stresses obtained from the model.

The start of expansion depended on the applied stress. The evolution of P_g was proportional to the strains. The increase of the stress in 5 mm thick steel rings was more significant because the rigidity slowed the radial strain (for the same applied stress). The more restrained the cylinder was, the faster the radial stress increased (Fig. 7). At 650 days, the gel pressure, representing the average pressure transferred to the aggregate surface, varied from 4.6 MPa to 10.0 MPa according to the stress state (Fig. 8). As expected from the model equations, the maximum pressure was obtained for the concrete with the greatest loading (20 MPa) and restraint (5 mm). From 350 days to the end of these experiments, stresses decreased. Shrinkage became the main phenomenon in this period.

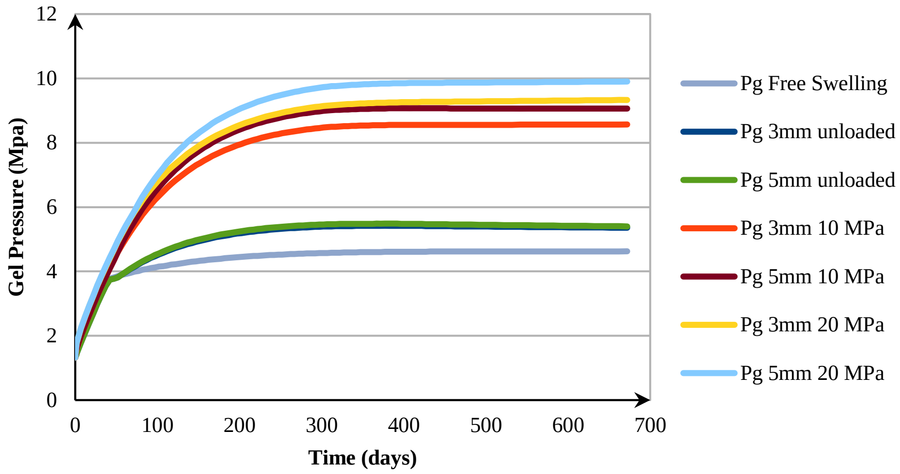

Fig. 8. Gel pressure from the model in tests.

4. Impact of restraint

Based on calibration using Multon's tests, the model reproduced the effects of stresses and restraints on ASR expansion faithfully. In these tests, the rigidity of the steel rings was not infinite. They were deformable whereas, in reality, restraint can be more rigid (in the case of a dam for example).

This part describes a theoretical test performed in order to analyse the effects of perfect restraint on ASR-expansion (displacement equal to zero in blocked directions). The aim was to compare the behaviours of expansive concrete with restraints or applied stress (in the next part). To facilitate the modelling of mechanical boundary conditions, a cube was modelled. It was restrained in from one to three directions (Table 4). In order to analyse the concrete behaviour under ASR-pressure only, the tests were calculated without shrinkage. This avoided problems of debonding between the boundary condition and the concrete. Stresses were applied after 28 days.

In Multon's free swelling test, the strain at 700 days approached 0.08 % (without shrinkage). For these theoretical tests, ASR maximum volume was fixed in order to obtain a usual but larger expansion - equal to 0.3%. Fig. **9** shows the calculations for a strain of 0.3% with a maximum gel volume $\phi_g^\infty = 0.03\ \mathrm{m}^3/\mathrm{m}^3$ and a fraction of non-effective gel $\phi_g^\infty = 0.008\ \mathrm{m}^3/\mathrm{m}^3$. Numerical tests in restrained conditions were performed with these parameters.

Swelling restrained in one direction	Swelling restrained in two directions	Swelling restrained in three directions
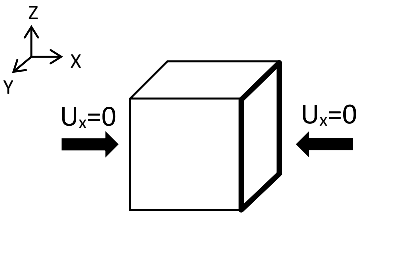	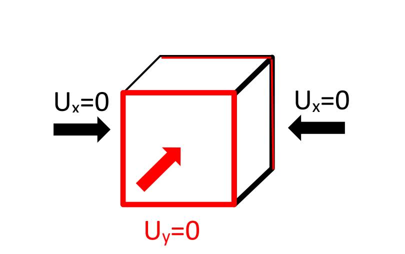	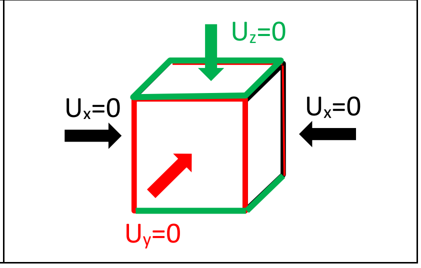

Table 4. Boundary conditions of theoretical tests.

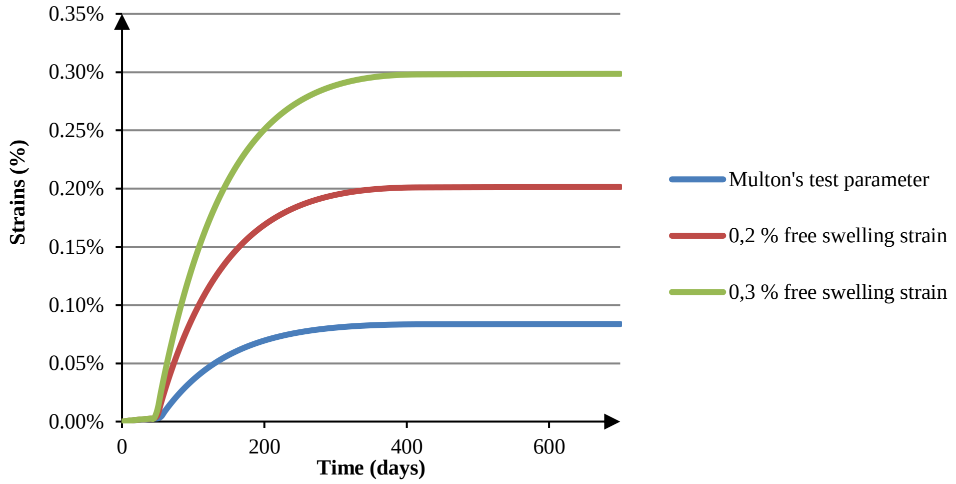

Fig. 9. Comparison of free swelling strains.

First, strains in free directions were compared (Fig.10). Strain in free directions increased by 25% compared to stress free expansion when the cube was restrained in one direction and by 65% when it was restrained in two directions.

After running a free swelling test and multi-direction perfectly restrained expansion tests, stresses were extracted (Fig. 11). The stress in restrained conditions could be described in two phases: a slow increase of the stress before first cracking (0 to 80 days), then fast increase after first ASR damage. For these conditions of perfect restraint, the maximum stress lay between 3 and 7 MPa of compression (for 1 to 3 restrained directions). It should be noted that final stress was not directly proportional to the number of restrained directions. Gel pressure rose strongly if three directions were restrained because this constituted full confinement. If the free maximal strain was 0.3%, an isotropic thermo-elastic calculation gave a stress of 113.1 MPa ($E_c.\varepsilon$=37700 * 0.003). Taking usual standard creep into account with an effective Young's modulus (E_c= E_{c0}/3), the result was still 37.7 MPa. These results are not consistent with experimental results [10]. Finally, it is very interesting to note the good agreement between the compressive stress of 3 MPa obtained for 1 D restraint and stresses usually observed in dams restrained in one direction [26]. This is also a good justification for using this type of modelling to represent anisotropy of expansion with stresses in real structures.

For specimens with 2 or 3 restrained directions, the maximum compressive stress increased, reaching 4 and 7 MPa respectively. This result depended on the capacity of ASR-gels to move in the concrete porosity. Under such pressures, ASR-gels could permeate further through aggregate and concrete porosity than in the stress free conditions taken into account in the pressure equation (8).

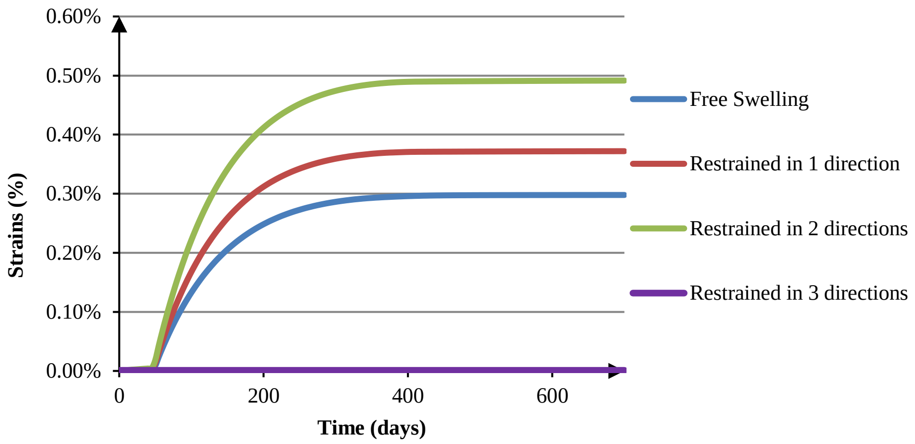

Fig.10. Comparison of strains in free swelling and restrained tests.

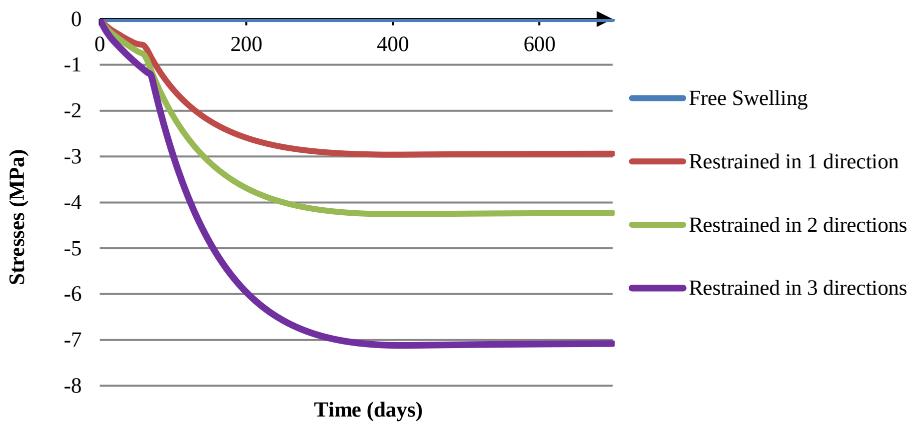

Fig. 11. Comparison of stresses in free swelling and restrained tests.

In the next part, stresses obtained in these tests are applied instead of restraints to analyse the differences between the effect of restraint and the effect of stress on ASR-expansion. For example, for the 3-direction restrained tests, stresses are applied from 0 to 7 MPa in these directions.

5. Impact of stresses

5.1. Compressive stress

Many structures (prestressed ones for example) are subjected to compressive stresses before ASR swelling appears. The aim of this part is to compare the behaviours of restrained structures and structures subjected to stress during ASR swelling.

For the specimen restrained in one direction, induced stresses were between 0 and 3 MPa. Here, they were applied in increments of 0.5 MPa. Fig. 12 shows the strains obtained for different loads in the stress direction. The larger the applied stress, the smaller the final strain. Above 1 MPa of compressive stress, the latency period depended on the stress state because creep strains were larger than the strains induced by the gel pressure. This period varied from 50 to 245 days. For the 3 MPa test (close to the maximum pressure obtained in the restrained test), the final strain was close to 0. Strain decreased proportionally to applied stress. The modelling was thus consistent when expansions under restraint and under applied stress were compared. According to the stress amplitude and ASR-latency time, creep was first predominant in the concrete behaviour. The final difference between restrained and applied stress tests was due to creep. The 5 MPa case (Fig. 12) showed that there was no swelling after a compressive stress threshold (here between 3 and 5 MPa). There was no cracking in the loading direction. In Larive's tests [14], a 5 MPa uniaxial compressive stress was applied to the specimen. Cracks only appeared parallel to the loading direction, while cracking was isotropic in the stress free specimen.

Fig. 13 shows the damage in the loaded and free directions for the 3 MPa loading test (one direction loaded). The first damage was in the unloaded direction and then the loaded direction was slightly damaged (here for a coefficient $h_{asr} = 0.03$). There was a delay between the start of cracking in the different directions, as explained in Fig. 3. The free direction was less damaged than the loaded direction. This represents the effect of compressive stress on the anisotropy of cracking due to ASR-expansion. The difference depends directly on the applied stress. For a smaller stress, the damage perpendicular to the loaded direction is greater while, for a stress higher than about 3 MPa, we can expect to obtain no damage perpendicular to the loaded direction. As damage directly affects the Young's modulus, the material becomes anisotropic; the Young's modulus will be smaller in the free direction while the mechanical performances are less affected in the loaded ones.

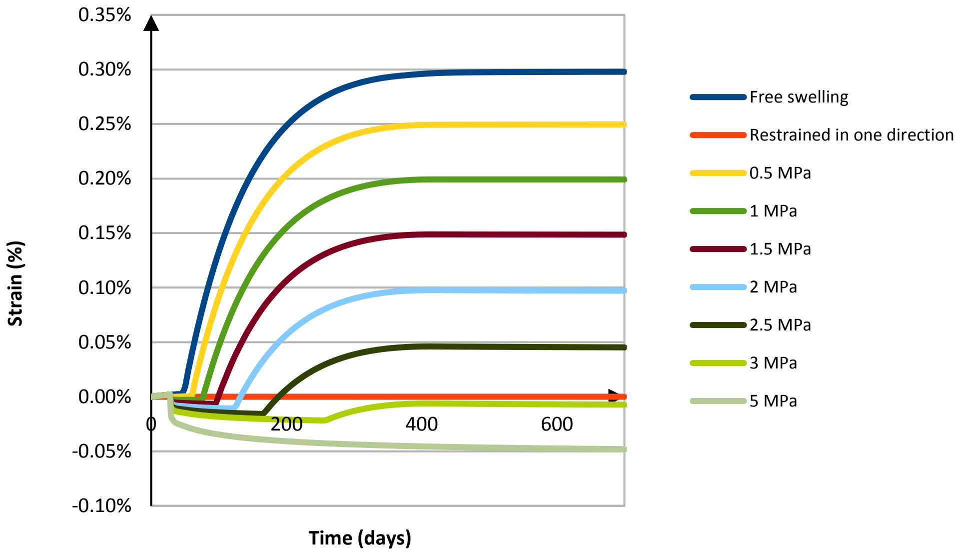

Fig. 12. Strains in loaded or restrained direction.

ASR damage is not linearly proportional to the stress applied (Fig. 14) and, in the model, the material parameter $\varepsilon^{k,isr}$ (ASR characteristic strain) allows this phenomenon. It weights ASR plastic strains when calculating ASR damage (13). Furthermore, when the stress was applied, gel pressure had to reach a higher value in order to exceed the cracking criteria. This took time and damage became delayed. When the specimen was restrained in one direction, it became damaged more rapidly as soon as the swelling began but the damage development was slowed down because the induced compressive stress also increased slowly. Finally, restraint test specimens can be compared to reinforced structures and applied stress test specimens to concrete structures such as bridge piers or prestressed beams.

Numerical results on the effect of stress can be compared to those obtained with Charlwood's law [3] (17).

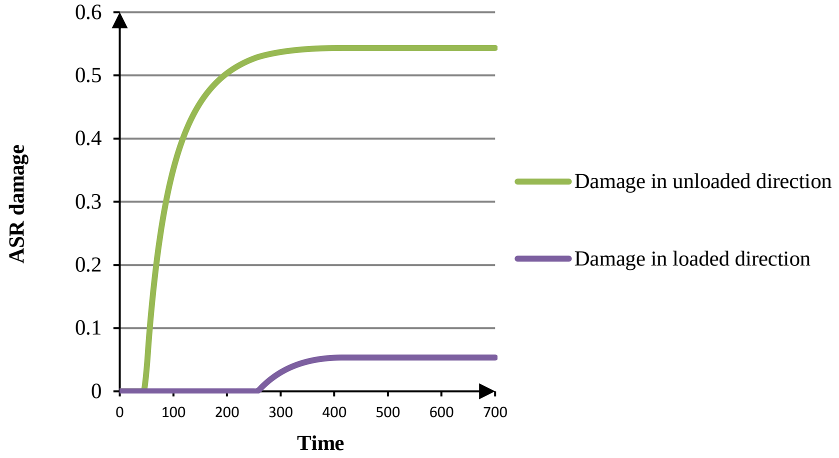

Fig. 13. ASR damage in the 3 MPa test (applied in one direction).

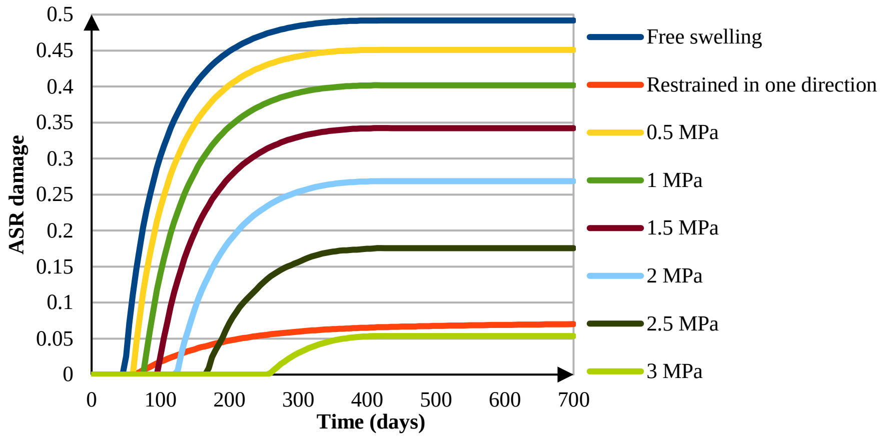

Fig. 14. Damage in loading direction (one direction loaded or restrained).

$$\varepsilon = \begin{cases} \varepsilon_u & if \;\; \sigma \leq \sigma_l \\ \varepsilon_u - K\, log_{10}\left(\dfrac{\sigma}{\sigma_l}\right) & if \;\; \sigma > \sigma_l \end{cases} \tag{17}$$

When the applied stress σ is smaller than the stress threshold σ_l, the strain is equal to ε_u (a material parameter). When the applied stress σ exceeds the threshold σ_l, the strain decreases from ε_u to zero. K is a material parameter that fits the slope of the decrease.

In Fig. 15, the parameter K from Charlwood's law has been fitted with the least squares method on 1D model results (K = 0.0027, $\varepsilon_u = 0.003$, $\sigma_l = 0.3\ MPa$). Charlwood's law is more non-linear than this model (Fig. 15) and it does not consider differences of behaviour between uniaxial and multi-axial loading. For this fitting, Charlwood's law strain is close to the model in 1D for small stresses (< 3 MPa). In the 2D case, the stress needed to obtain a strain equal to zero is nearly the same in both models (≈ 4 MPa). However, Charlwood's law gives more non-linear results for lower stresses. The model proposed here considers the confinement effect in the gel pressure equation (Eq. 18). This explains some differences between 1D, 2D and 3D.

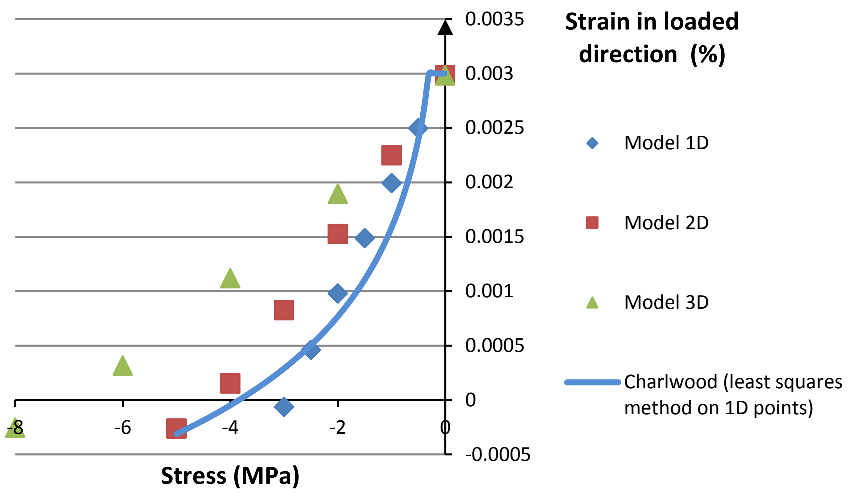

Fig. 15. Strains obtained from the model in multi-axial loadings
and from Charlwood's law [3].

5.2. *Impact of unloading*

In this part, the impact of unloading during swelling is studied. When an owner tries to understand the ASR damage in his damaged structure, core drilling is often used. This action leads to a relaxation of stresses in the sample taken. It can also represent the breaking of a prestressed bar. The material used here was the same as in part A. Specimens were loaded at 28 days and unloaded at 200 days (for an ASR-advancement of about 0.7).

In the loaded direction, strains were negative after application of the load, because of concrete creep, and before ASR swelling, according to the applied stress value (Fig. 16). When the material was unloaded, the strain in this direction occurred very fast and tended towards the free swelling strain value. This result confirms the analysis performed in [27].The final difference between free swelling and unloaded tests strains was small but proportional to the applied stress. It was due to the irreversible creep strain reached before swelling. When the stress was removed, strain in the initially unloaded direction stopped growing and all the swelling went to the initially loaded direction (Fig.

17). At this time, the ASR criterion in the initially loaded direction was reached instantly: it passed from $\widetilde{\mathrm{R}}_{\mathrm{I}}^{\mathrm{g}} - \sigma$ to $\widetilde{\mathrm{R}}_{\mathrm{I}}^{\mathrm{g}}$, the tensile strength of the concrete (Fig. 3). There was a jump in displacement.

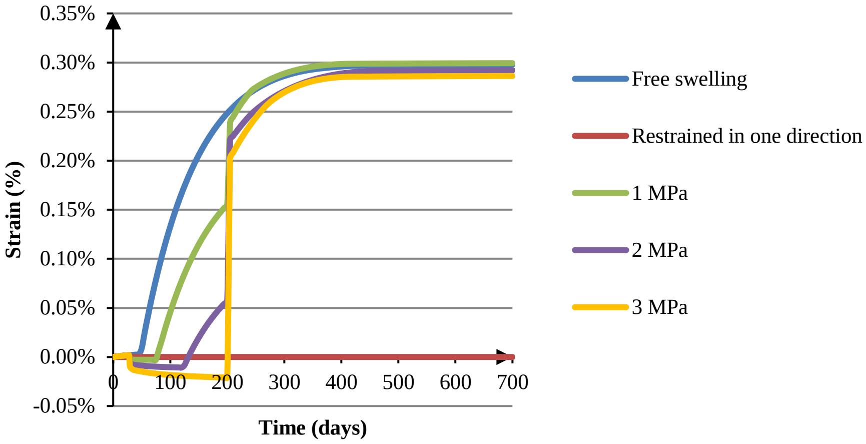

Fig. 16. Strains in initially loaded direction.

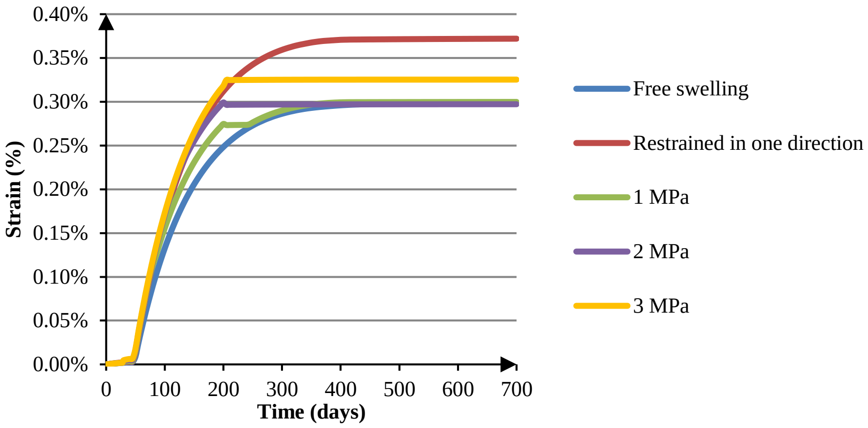

Fig. 17. Strains in initially unloaded direction.

In the initially unloaded direction (Fig. 17), at 200 days, strains decreased slightly. When strong swelling is in progress on an initially loaded direction, ASR plastic strains $\varepsilon^{p,g}$ increase fast. In (8, this strain directly impacts the mean gel pressure, which decreases abruptly (Fig. 18). Therefore, the ASR strain lost part of its elastic strain. This explains the decreased strains in the initially unloaded direction. In reality, this effect can be decreased by ASR-gel exudations as noted by [28]. When gels permeate out of drilled cores, pressure decreases brutally and expansion can slow down and stop. In any case, this modifies the expansive behaviour of the concrete.

Due to stress release and its impact on expansion, unloading could imply high ASR damage in the initially loaded direction (Fig. 19) whereas there was no damage in this direction when the concrete was under loading in the structure. In consequence, new damage could be encouraged by unloading or drilling. Mechanical or residual expansive tests, performed with such drilled cores, could be negatively impacted by this damage, which is not really present in the structure. Using such a test for predictive calculations could then be hazardous.

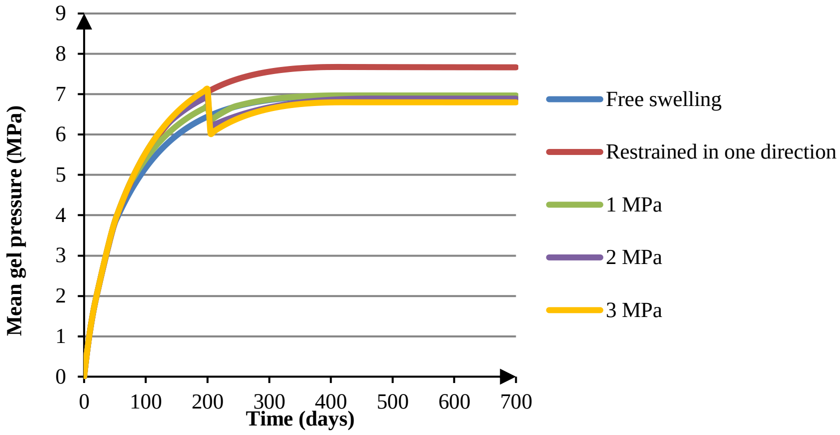

Fig. 18. Gel pressure variation in unloading tests.

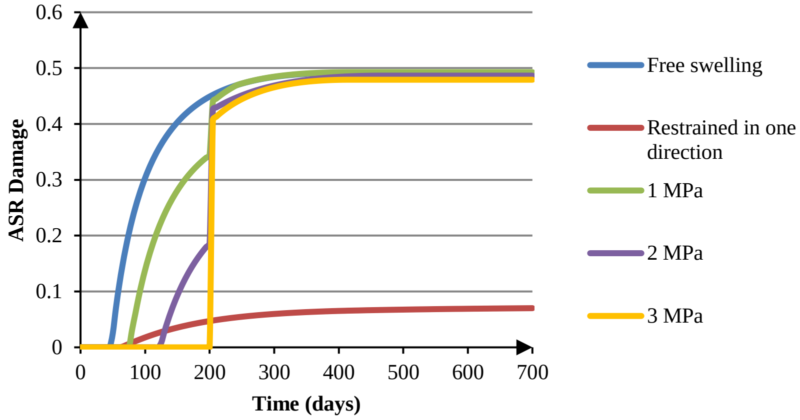

Fig. 19. ASR damage in initially loaded direction.

5.3. Tensile stress

In order to complete the theoretical analysis, the same kinds of tests were performed with tensile stress. Here, specimens were loaded in one direction only with tensile stresses of 0.5 and 1 MPa (a higher value cannot converge due to coupling of the tensile damage with ASR damage, which leads to specimens cracking). Strains in the loaded direction are summarized and compared to free swelling in Fig. 20. First, it is important to note that tensile stress accelerated the ASR swelling (Fig. 21). This can be explained by the ASR plastic criterion being reached sooner for tensile stress. Secondly, the final strain induced by expansion in concrete subjected to tensile stresses increased (Fig. 20). In real structures, tensile stresses can be induced by moisture gradients and restrained. Thus, in reinforced concrete, the tensile cracking criterion could be reached first, due to restrained shrinkage before ASR expansion. This could finally accelerate the apparition of the first expansion compared to stress free conditions. However, once swelling occurs, compressive stresses will rise due to expansion restraint and expansion will decrease compared to expansion without compressive stress.

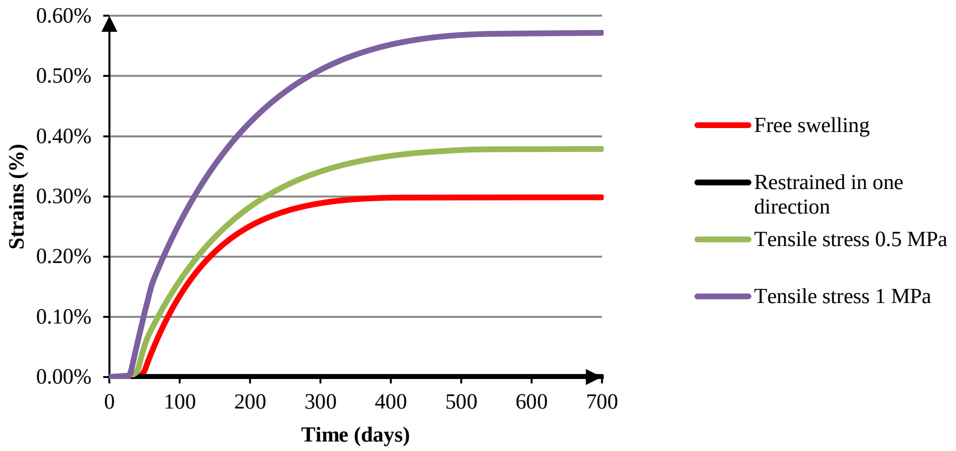

Fig. 20. Strains in restrained or loaded direction.

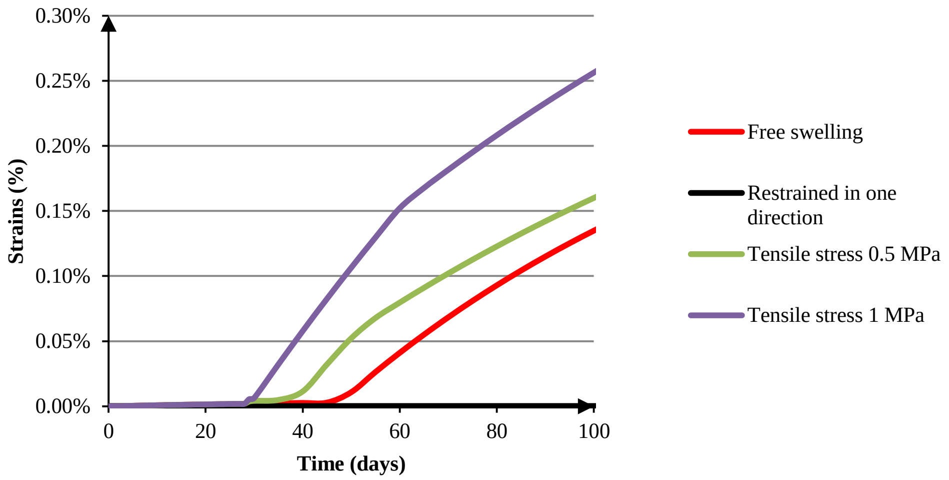

Fig. 21. Strains in restrained or loaded direction (zoom on 0-100 days).

Consecutively, ASR damage increased with the load in loaded directions (Fig. 22) as the solid skeleton had to support concurrent stresses: gel pressure and structural stress. Damage was non-linear because of the ASR characteristic strain $\varepsilon^{k,isr}$(13).

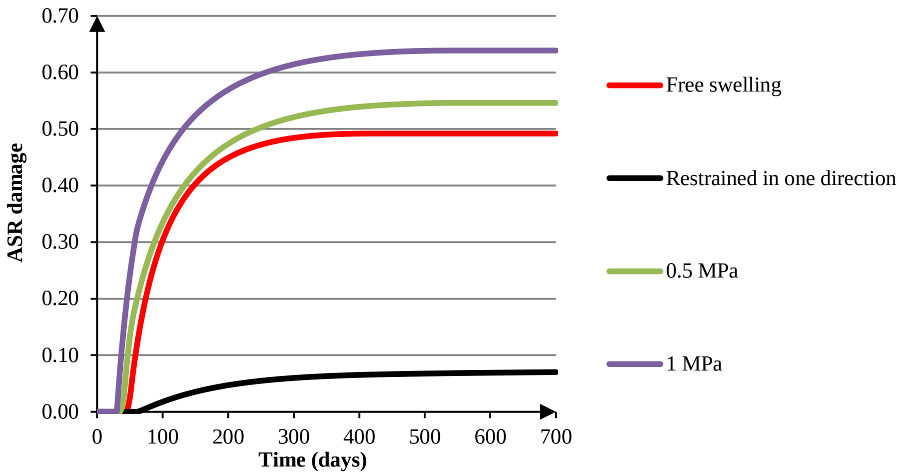

Fig. 22. ASR damage in restrained or loaded direction.

6. Impact of reinforcement on ASR-expansion

In many damaged structures, the effect of stresses on ASR expansion is mainly due to restraint by reinforcement. In this part, the impact of reinforcement on specimens subjected to ASR is analysed on the basis of the calibration obtained for Multon's tests, which quantified the impact of stresses on ASR-expansion. The focus is particularly on the anisotropic effect of reinforcement and on induced stresses.

In order to approach the behaviour of structures, real conditions were simulated: the shrinkage was taken into account and steel was used instead of perfect restraints. The main specimen was a concrete cylinder 1 metre high and 13 centimetres in diameter (Table 5). First, free swelling gave a reference of isotropic values for damage and strain. Then, anisotropy was induced by longitudinal ribbed bars and steel rings, which could represent the effect of stirrups on expansion. One test consisted of adding a longitudinal ribbed steel bar (diameter 12 mm, i.e. 0.85% of steel section) in the centre of the specimen. Another one consisted of adding steel rings (8x8 mm section) every 10 centimetres. The last test was performed with both the longitudinal ribbed bar and the steel rings (Table 5).

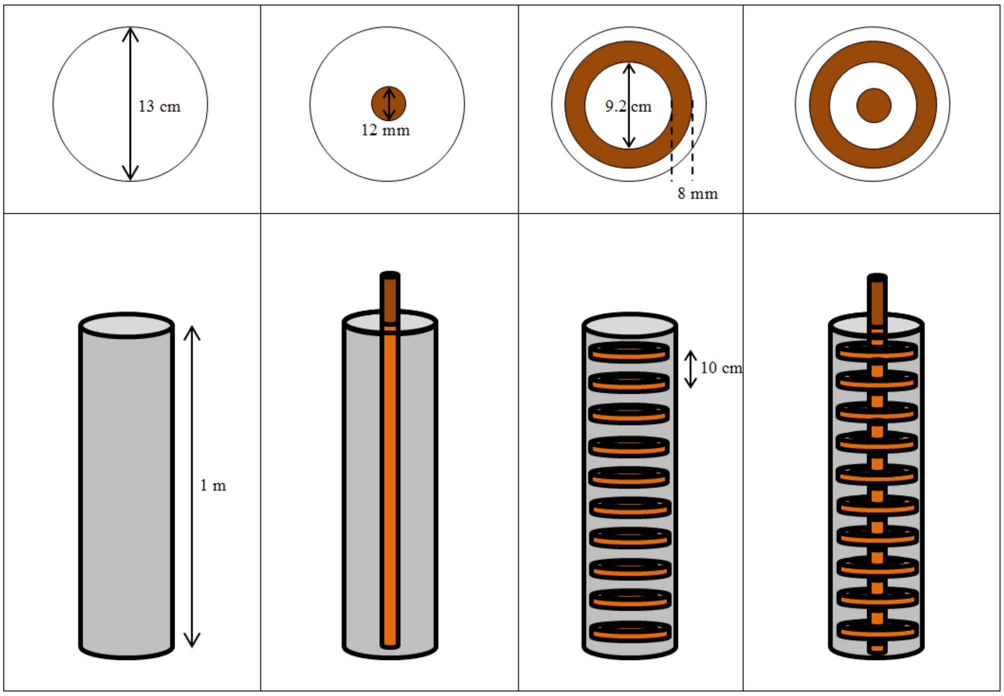

Table 5. Scheme of specimen geometries.

In terms of anisotropy, the ratio of the longitudinal and transversal strains (respectively ε_L and ε_T) to the longitudinal and transversal strains in the free expansion condition (ε_{WR}) were compared for each test (Table 6). The longitudinal ribbed bar had a strong impact on longitudinal strain: about 50% of its initial value. The transversal strain increased by 20%. In the case of steel rings, longitudinal strain increased (30%) while transversal strain decreased (to 50% between the longitudinal axis and the rings). When both reinforcements were used, longitudinal strains were reduced to half (between 40 and 60% of the free swelling value). Transversally, the difference depended on the location: between the ribbed bar and a ring, concrete was confined and strains were reduced by 35%. However, between two rings, strains grew due to the reinforcement in the transversal direction, as restrained parts helped to increase the strain in this direction. These results are drawn on the deformed shapes of specimens in Table 7.

Table 6 also gives stress values inside the concrete and the steel. In concrete, the confinement increased the compression stress value (from 0 to 3.3 MPa). In the steel bar, stress could reach 300 MPa when the confinement was strong. Here, it is not sufficient to induce lamination of the steel but it is primordial if the steel is designed as a structural part.

	Without Reinforcement (WR)	Ribbed bars (12 mm)	Steel rings (8 mm)	Ribbed bars and steel rings
$\frac{\varepsilon_L}{\varepsilon_{WR}}$	1	From 0.3 *(close to the top)* to 0.5 *(close to the axis of symmetry)*	1.3	From 0.4 *(close to the top)* to 0.6 *(close to the axis of symmetry)*
$\frac{\varepsilon_T}{\varepsilon_{WR}}$	1	1.2	From 0.5 *(inside a ring)* to 1.0 *(between rings)*	From 0.65 *(inside a ring)* to 1.25 *(between rings)*
$\sigma_{MIN\ concrete}$ (MPa)	0	-1.8 *(parallel to the longitudinal axis)*	-0.7 *(perpendicular to the longitudinal axis)*	-3.3 *(between the bar and a ring)*
$\sigma_{MAX\ steel}$ (MPa)	-	195	110	300

Table 6. Test results.

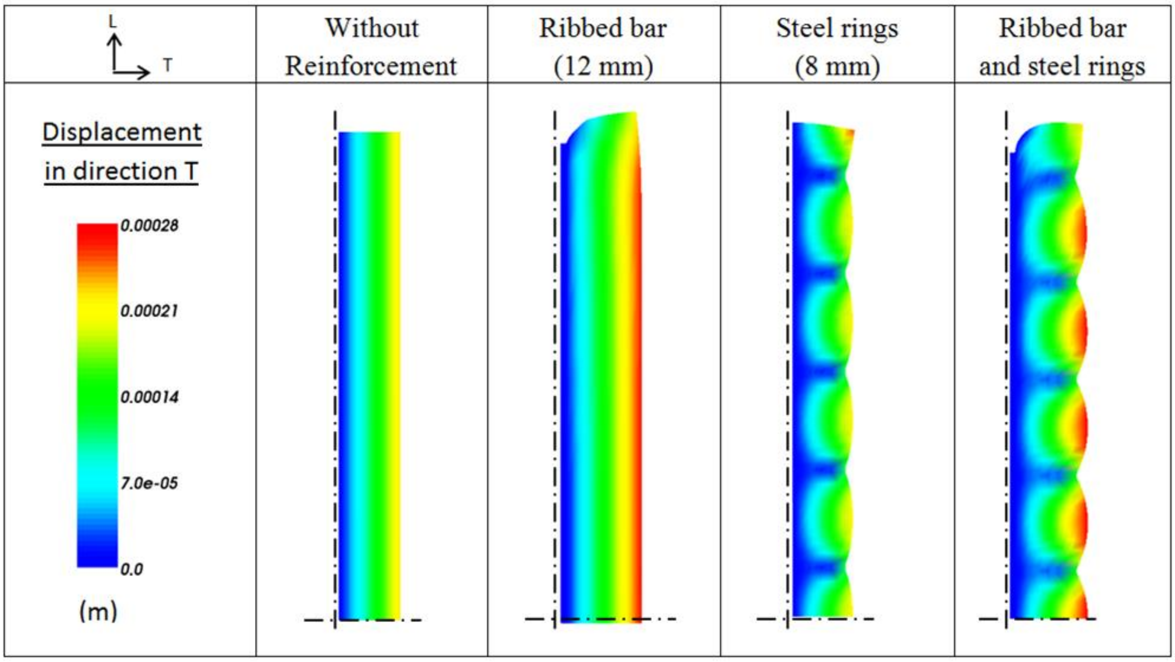

Table 7. Displacement in transversal direction T, drawn on the deformed shape.

Table 8 shows the distribution of longitudinal and transversal ASR plastic strains (respectively $\varepsilon^{pl}_{L\ ASR}$ and $\varepsilon^{pl}_{T\ ASR}$) on a quarter of the geometry (symmetrical conditions). ASR damage, and thus the impact of ASR on the mechanical properties of the concrete, can be calculated from these plastic strains with (13): a plastic strain of 0.3% corresponds to ASR damage of 0.5. In the longitudinal ribbed bar test, transversal ASR strains $\varepsilon^{pl}_{T\ ASR}$ were high in the steel-concrete contact zone because the steel bar restrained the swelling concrete in the other direction. This zone acted like a joint and expansion caused a debonding effect. This result is consistent with experimental results, which exhibit a decrease of ultimate bonding strength in the case of specimens without stirrups [29–31]. For the steel rings test, the maximum ASR plastic strain occurred near the rings in the longitudinal direction. The swelling was restrained in the transversal direction and strains were thus mainly longitudinal in that place because of anisotropy. This implies considerable damage in the longitudinal direction (transversal cracks). In the transversal direction, the maximum plastic strain was far from the steel rings as the swelling of the external concrete was restrained by the rigidity of the rings. When the ribbed bar and steel rings were used together, the debonding effect was still noticeable but just between rings. The rings restrained material expansion in the core of the specimen, which prevented debonding of the longitudinal bar. There was less damage inside the steel rings due to confinement by the bar. However, there was more damage outside because the concrete strains between the rings were greater than in the previous test. According to the importance of restraint (number of stirrups compared to the concrete section), the ultimate bonding strength could increase as observed qualitatively in [29]. Otherwise, cracking could be delayed under external loads thanks to ASR prestressing in reinforced structures. Experimentally, a reinforced wall was affected by ASR cracks later than a sound one [32].

It is interesting to analyse the effect of reinforcement on cracking anisotropy and the impact on the analysis of structures for future prognosis. Table 8 shows two core samples drilled in the same place in specimens in stress free conditions (marked as 1 in Table 8) and with a longitudinal ribbed bar (marked 2). The first sample, taken in the free swelling test exhibits ASR isotropic damage of about 0.5 (corresponding to a plastic strain of 0.3%). The second one, extracted from the longitudinal ribbed bar test, exhibits ASR cracks mainly oriented parallel to the bar (ASR damage: 0.65). Due to restraint, ASR damage in the other direction is about 0.35. Thus, if these cores were used to measure the residual mechanical strength of concrete, the core drilled in stress free conditions would lead to a decrease of 50% while the core drilled perpendicular to the reinforcement would lead to a decrease of 65% and the core drilled parallel to the reinforcement to a decrease of only 35%. Usually, affected concrete properties are assessed from compression tests; therefore compressive damage is smaller than tensile damage (14). For instance, the last tensile damage (65% and 35%) corresponded respectively to compressive damage of 27% and 12%. This difference is obviously important for future calculations since underestimating the Young's modulus can lead to a large overestimate of the structure deflection.

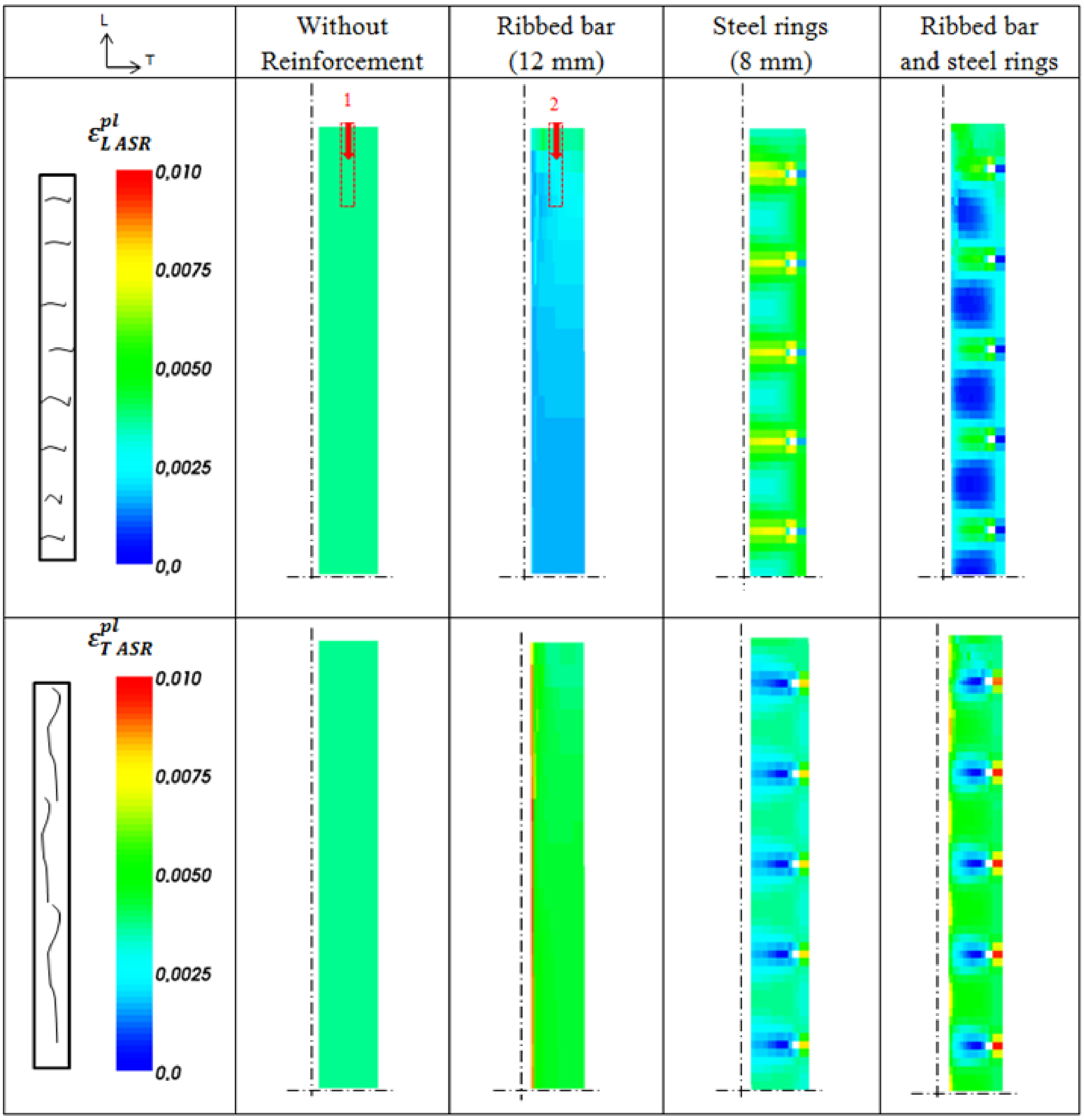

Table 8. Final ASR plastic strains obtained from tests.

The behaviour of reinforced samples and the impacts of compressive and tensile stresses on ASR-expansion have been explained. The flexural behaviour of ASR-damaged beams can be deduced of the previous analysis. In reinforced structures, the steel bars imply expansion restraint and thus chemical presstress. From Table 6, it can reach about 1.8 MPa to 3.3 MPa depending on stirrups distribution. Theses stresses due to restrained expansion leads to an increase of the tensile strength and to a decrease of the compressive strength in the reinforced structures. When the loading is applied, the stress necessary to cause the cracking of the concrete is the tensile concrete strength plus the chemical prestress. Compared to a non-reactive reinforced beam, mechanical cracking due to flexion is delayed since the loading necessary to cause the cracking of the part of the structure in tension is higher. This behaviour is confirmed experimentally [33] . In the parts in compression, the compressive strength is decreased (about 1.8 MPa to 3.3 MPa). Indeed, structural cracking in uniaxial compressive test without ASR is due to dilatancy in unloaded directions, it is called a shear damage. ASR expansion is restrained by the reinforcement, strains are transferred in the other directions (Fig. 13). So, the compressive strength is reduced in the parts of the structures submitted to compression. It could have an impact on the final break of the beam but it is often negligible because the compressive strength is often about ten times higher than the chemical prestress. Furthermore, for prestressed beams, the flexural behaviour explained for reinforced beams is similar: the benefit is improved on the part in tension and the compressive strength is reduced.

7. Conclusion

The aims of this paper were to show how restraint and stress can modify ASR expansion and to propose a model able to take this effect into account. First, the model was presented. It considers both ASR mechanisms and physical phenomena, such as creep, damage and their coupling, so as to be representative of concrete behaviour. Attention was focused on the gel pressure and on the hardening law chosen to manage the cracking due to ASR. The gel pressure calculation took elastic strains and ASR plastic strains into account in order to respect the principles of poromechanics when representing cracks.

The model was calibrated and validated on experimental results [10]. Specimens were tested under several mechanical conditions: creep and shrinkage without ASR, free swelling with or without loads, restrained swelling (with 3 and 5 mm thick steel rings) with or without longitudinal loading. The calculations show numerical results that are realistic when compared to experimentation.

Based on this calibration, a theoretical analysis was carried out:

1. The comparison of expansion under restraint and stresses pointed out the importance of loading chronology in ASR kinetics.
2. For a final expansion of about 0.3%, a maximum stress of about 3 MPa is reached in the case of expansion that is perfectly restrained in only 1 direction. This seems realistic compared to field experience [26].
3. For a specimen restrained in three directions, the maximum compressive stress can be expected to be greater and reached about 7 MPa in this work (for a stress free expansion of 0.3%). This result will depend on the capacity of ASR gels to move in the porosity of concrete aggregate, which is taken into account in the gel pressure equation.
4. Simulated unloading tests during swelling showed that specimens extracted from a structure could crack rapidly due to the relaxing of stress and thus would impact future prognostic tests.
5. Tension stresses during ASR swelling could lead to premature and greater expansion.

Finally, restrained tests were carried out with steel reinforcement (longitudinal ribbed bar and transversal steel rings). They enabled conclusions to be drawn on ASR development in reinforced structures and could help experts in the management of ASR reinforced and damaged structures. The combination of coring direction with cracking anisotropy can lead to differences in the analysis of structures. For a reinforced structure, the stress state can induce anisotropic cracking that leads to weak and strong zones of material which depend on the loading or restraint directions. Basing a prognosis on such tests (residual expansion tests and / or mechanical tests on cores drilled from structures) could thus lead to the structural consequences of ASR being poorly estimated.

REFERENCES

[1] E. Bourdarot, A. Sellier, S. Multon, E. Grimal, A review of continuum damage modelling for dam analysis, European Journal of Environmental and Civil Engineering. 14 (2010) 805–822. doi:10.1080/19648189.2010.9693263.

[2] R.G. Charlwood, Predicting the Long Term Behaviour and Service Life of Concrete Dams, in: Graz, Austria, 2009. http://civil.colorado.edu/~saouma/AAR/Library/Paris-2009/Charlwood/Predicting-long-term.pdf (accessed July 29, 2016).

[3] R.G. Charlwood, S.V. Solymar, D.D. Curtis, A review of alkali aggregate reactions in hydroelectric plants and dams, in: Proceedings of the International Conference of Alkali-Aggregate Reactions in Hydroelectric Plants and Dams, 1992.

[4] RILEM Technical Comitee 259-ISR, Benchmark/Round Robin Analyses : ASR Prognosis of deterioration and loss of serviceability in structures affected by alkali-silica reactions, (2016). http://www.rilem.net/global/gene/doc_link.php?doc=2016161048_rilem-tc-259-isr-wg2-benchmark.pdf (accessed July 29, 2016).

[5] N. Baghdadi, F. Toutlemonde, J.-F. Seignol, Modélisation de l’effet des contraintes sur l’anisotropie de l’expansion dans les bétons atteints de réactions de gonflement interne, in: Conférence AUGC, Bordeaux, 2007. http://www.iut.u-bordeaux1.fr/gc/augc07/index/pdf/BCM/Baghdadi.pdf (accessed May 3, 2016).

[6] C. Comi, R. Fedele, U. Perego, A chemo-thermo-damage model for the analysis of concrete dams affected by alkali-silica reaction, Mechanics of Materials. 41 (2009) 210–230. doi:10.1016/j.mechmat.2008.10.010.

[7] E. Grimal, A. Sellier, S. Multon, Y. Le Pape, E. Bourdarot, Concrete modelling for expertise of structures affected by alkali aggregate reaction, Cement and Concrete Research. 40 (2010) 502–507. doi:10.1016/j.cemconres.2009.09.007.

[8] P. Léger, P. Côté, R. Tinawi, Finite element analysis of concrete swelling due to alkali-aggregate reactions in dams, Computers & Structures. 60 (1996) 601–611. doi:10.1016/0045-7949(95)00440-8.

[9] V. Saouma, L. Perotti, Constitutive model for alkali-aggregate reactions, ACI Materials Journal. 103 (2006) 194.

[10] S. Multon, F. Toutlemonde, Effect of applied stresses on alkali–silica reaction-induced expansions, Cement and Concrete Research. 36 (2006) 912–920. doi:10.1016/j.cemconres.2005.11.012.

[11] E. Grimal, A. Sellier, Y. Le Pape, E. Bourdarot, Creep, Shrinkage, and Anisotropic Damage in Alkali-Aggregate Reaction Swelling Mechanism-Part I. A Constitutive Model, ACI Materials Journal. 105 (2008) 227–235.

[12] A. Sellier, S. Multon, L. Buffo-Lacarrière, T. Vidal, X. Bourbon, G. Camps, Concrete creep modelling for structural applications: non-linearity, multi-axiality, hydration, temperature and drying effects, Cement and Concrete Research. 79 (2016) 301–315. doi:10.1016/j.cemconres.2015.10.001.

[13] M.A. Biot, General Theory of Three-Dimensional Consolidation, Journal of Applied Physics. 12 (1941) 155–164. doi:10.1063/1.1712886.

[14] C. Larive, Apports combinés de l'expérimentation et de la modélisation à la compréhension de l'alcali-réaction et de ses effets mécaniques, phdthesis, Ecole Nationale des Ponts et Chaussées, 1997. https://pastel.archives-ouvertes.fr/tel-00520676/document (accessed May 3, 2016).

[15] J. Moon, S. Speziale, C. Meral, B. Kalkan, S.M. Clark, P.J.M. Monteiro, Determination of the elastic properties of amorphous materials: Case study of alkali–silica reaction gel, Cement and Concrete Research. 54 (2013) 55–60. doi:10.1016/j.cemconres.2013.08.012.

[16] A. Leemann, P. Lura, E-modulus of the alkali–silica-reaction product determined by micro-indentation, Construction and Building Materials. 44 (2013) 221–227. doi:10.1016/j.conbuildmat.2013.03.018.

[17] T. Adachi, S. Sakka, Dependence of the elastic moduli of porous silica gel prepared by the sol-gel method on heat-treatment, J Mater Sci. 25 (1990) 4732–4737. doi:10.1007/BF01129933.

[18] Z. Bažant, G. Zi, C. Meyer, Fracture Mechanics of ASR in Concretes with Waste Glass Particles of Different Sizes, Journal of Engineering Mechanics. 126 (2000) 226–232. doi:10.1061/(ASCE)0733-9399(2000)126:3(226).

[19] C.F. Dunant, K.L. Scrivener, Effects of uniaxial stress on alkali–silica reaction induced expansion of concrete, Cement and Concrete Research. 42 (2012) 567–576. doi:10.1016/j.cemconres.2011.12.004.

[20] S. Multon, F. Toutlemonde, Effect of moisture conditions and transfers on alkali silica reaction damaged structures, Cement and Concrete Research. 40 (2010) 924–934. doi:10.1016/j.cemconres.2010.01.011.

[21] H. Kagimoto, Y. Yasuda, M. Kawamura, ASR expansion, expansive pressure and cracking in concrete prisms under various degrees of restraint, Cement and Concrete Research. 59 (2014) 1–15. doi:10.1016/j.cemconres.2014.01.018.

[22] B. Capra, A. Sellier, Anisotropic modelling of alkali–aggregate reaction in concrete, in: Quebec City, 2000: pp. 929–938.

[23] A. Sellier, B. Bary, Coupled damage tensors and weakest link theory for the description of crack induced anisotropy in concrete, Engineering Fracture Mechanics. 69 (2002) 1925–1939. doi:10.1016/S0013-7944(02)00069-3.

[24] L.F.M. Sanchez, S. Multon, A. Sellier, M. Cyr, B. Fournier, M. Jolin, Comparative study of a chemo–mechanical modeling for alkali silica reaction (ASR) with experimental evidences, Construction and Building Materials. 72 (2014) 301–315. doi:10.1016/j.conbuildmat.2014.09.007.

[25] M.T. Van Genuchten, A Closed-form Equation for Predicting the Hydraulic Conductivity of Unsaturated Soils1, Soil Science Society of America Journal. 44 (1980) 892. doi:10.2136/sssaj1980.03615995004400050002x.

[26] P. Rivard, G. Ballivy, C. Gravel, F. Saint-Pierre, Monitoring of an hydraulic structure affected by ASR: A case study, Cement and Concrete Research. 40 (2010) 676–680. doi:10.1016/j.cemconres.2009.09.010.

[27] M. Alnaggar, G. Cusatis, G.D. Luzio, Lattice Discrete Particle Modeling (LDPM) of Alkali Silica Reaction (ASR) deterioration of concrete structures, Cement and Concrete Composites. 41 (2013) 45–59. doi:10.1016/j.cemconcomp.2013.04.015.

[28] P. Rivard, F. Saint-Pierre, Assessing alkali-silica reaction damage to concrete with non-destructive methods: From the lab to the field, Construction and Building Materials. 23 (2009) 902–909. doi:10.1016/j.conbuildmat.2008.04.013.

[29] P.S. Chana, BOND STRENGTH OF REINFORCEMENT IN CONCRETE AFFECTED BY ALKALI SILICA REACTION, TRRL CONTRACTOR REPORT. (1989). https://trid.trb.org/view.aspx?id=314058 (accessed July 29, 2016).

[30] P.S. Chana, G.A. Korobokis, THE STRUCTURAL PERFORMANCE OF REINFORCED CONCRETE AFFECTED BY ALKALI SILICA REACTION: PHASE II, (1992). https://trid.trb.org/view.aspx?id=369872 (accessed July 29, 2016).

[31] S.R. Rigden, Y. Majlesi, E. Burley, BOND STRESS FAILURE IN ALKALI SILICA REACTIVE REINFORCED CONCRETE BEAMS, in: 1992. https://trid.trb.org/view.aspx?id=450549 (accessed July 29, 2016).

[32] F. Habibi, S.A. Sheikh, N. Orbovic, D.K. Panesar, F.J. Vecchio, ALKALI AGGREGATE REACTION IN NUCLEAR CONCRETE STRUCTURES: PART 3: STRUCTURAL SHEAR WALL ELEMENTS, in: Manchester, UK, 2015.

[33] S. Multon, J.-F. Seignol, E. Bourdarot, A. Jeanpierre, F. Toutlemonde, Effets structuraux de l’alcali-réaction: Apports d’une expérimentation sur éléments de structures à la validation de modèles, Revue Européenne de Génie Civil. 9 (2005) 1219–1247. doi:10.1080/17747120.2005.9692808.